Acta Materialia 313 (2026) 122305

Contents lists available at ScienceDirect

Acta Materialia

journal homepage: www.elsevier.com/locate/actamat

Full length article

Decoupling the effects of temperature and stress on grain growth in nanocrystalline Ni films

Yichen Yang [a,*], Yazhuo Liu [a], Ting Zhu [a], Olivier Pierron [a], Josh Kacher [b]

[a] Woodruff School of Mechanical Engineering, Georgia Institute of Technology, Atlanta, GA 30332, USA
[b] School of Materials Science and Engineering, Georgia Institute of Technology, Atlanta, GA 30332, USA

ARTICLE INFO

Keywords:
Grain growth
Texture evolution
Plasticity
Thin film
STEM

ABSTRACT

Understanding the interplay among microstructure, stress and temperature in controlling microstructural stability remains challenging. Here, we use in situ transmission electron microscopy (TEM) annealing and micro-electromechanical-system (MEMS)-based tensile testing to track grain-scale evolution in 100 nm-thick nanocrystalline Ni films with three different initial textures. Thermal annealing at 700 °C causes conventional grain growth driven by surface and grain boundary energy minimization, producing annealing twins and a strong ⟨111⟩ out-of-plane texture. In contrast, stress-induced texture evolution is strongly influenced by the initial microstructure. Grain-resolved statistics from 4D-STEM orientation mapping of over 100,000 grains reveal that stress alters grain growth through two distinct mechanisms. At ambient temperatures, differential yielding drives the growth of larger grains, resulting in size-biased coarsening. At 100 °C, stress helps grain boundaries overcome kinetic barriers, allowing low–surface-energy orientations to grow in a manner similar to thermally driven coarsening. Consequently, the final texture reflects the dominant grain growth mechanism, determined by the relative magnitudes of applied stress and temperature.

1. Introduction

Nanocrystalline (nc) metals exhibit superior strength relative to their coarse-grained counterparts due to the high density of grain boundaries (GBs) that impede dislocation motion. However, these same GBs also make nc metals prone to microstructural instability under thermal or mechanical loading. This instability typically manifests as grain coarsening, which in turn degrades mechanical performance by reducing strength [1,2].

In thin films, where free surfaces play a dominant role, grain growth at elevated temperatures is primarily driven by the reduction of both grain-boundary and surface energies [2–7]. Recent studies have also demonstrated that mechanical stresses can promote grain growth in nc metals, either in combination with elevated temperatures or even under ambient conditions [8–13]. In situ transmission electron microscopy (TEM) straining experiments on nc Ni thin films showed little grain growth under stress alone at room temperature, but when a modest tensile stress (~20% of yield strength) was applied concurrently with slight heating (~0.2 melting temperature T_m), rapid and discontinuous grain growth occurred [14]. Similarly, cyclic fatigue loading has been found to induce abnormal coarsening in nc and ultrafine-grained (ufg) Ni and Ni alloys, with large grains forming well before final failure [1–3,15]. Such observations confirm that an applied stress (either monotonic or cyclic) markedly enhances GB migration even at low temperatures, beyond what traditional curvature-driven grain growth models would predict.

The mechanistic origin of stress-assisted grain growth under plastic deformation, however, remains a subject of debate. On one hand, stress-assisted GB migration can be explained by the disconnection framework, in which the GB velocity is written as $v = M(\Gamma\kappa + \tau f(\beta, \hat{n}) + \psi)$ [16,17]. Here, M is the GB mobility, $\Gamma\kappa$ is the capillarity term, $\tau f(\beta, \hat{n})$ is the stress contribution arising from the character of GB disconnections and their shear-coupled motion, and ψ represents energy jumps across the boundary. Several studies have examined whether mechanical stress contributes directly to the thermodynamic driving force for grain-boundary migration in thin films. For instance, grain growth under cyclic loading at relatively low strain amplitudes (~0.18–0.3%) was observed to occur preferentially in grains with ⟨100⟩ axes aligned with the loading direction, consistent with elastic anisotropy [3]. A recent study quantitatively evaluated the competing driving forces

* Corresponding author.
E-mail address: yyang3025@gatech.edu (Y. Yang).

https://doi.org/10.1016/j.actamat.2026.122305
Received 10 December 2025; Received in revised form 28 April 2026; Accepted 30 April 2026
Available online 2 May 2026

governing texture transformation in Ag thin films by varying the applied stress during annealing and found that the resulting change in strain energy did not measurably affect the transformation kinetics [18]. Atomistic simulations indicate that mechanical work can act as a predominant driver for GB motion, even when other drivers (such as curvature) are absent [19]. Grain growth in nc Ni has been interpreted as a stress-relief mechanism without the need for significant dislocation activities [14]. Collectively, these results support the notion that stress can act as a direct thermodynamic driver for grain growth.

At the same time, stress can influence the mobility $M(\sigma,T)$. Stress can enhance GB mobility by lowering the activation barrier for shear-coupled disconnection glide or atomic shuffling at the boundary. The applied stress has been shown to activate shear-coupled GB migration and related mechanisms that increase boundary mobility [19,20]. The disconnection-based theory of GBs (i.e., treating GB disconnections as line defects with both step height and Burgers vector) predicts that even high-angle boundaries can support coupled motion, as confirmed by Cahn et al. and others [21]. In situ TEM deformation studies on UFG Al have further demonstrated GB migration velocities several orders of magnitude higher than those observed in purely thermal growth [22]. This observed behavior has been attributed to the combined effects of elevated grain-boundary mobility and grain rotation [22,23].

Given the diversity of driving forces, developing a mechanistic understanding of how microstructures evolve as a function of their initial state and applied thermal or mechanical conditions remains challenging. As the boundary network facets, coalesces, or twins, both the effective mobility and the driving force evolve irreversibly [24], causing the ensuing coarsening behavior to depend strongly on the sequence of microstructural events.

In this study, we aim to decouple the thermal and stress contributions to grain growth in freestanding nc Ni by independently varying temperature and stress using in situ TEM coupled with 4D-STEM orientation mapping. The 4D-STEM technique enables quantitative tracking of microstructural evolution through both statistical analysis of over 100,000 grains and grain-resolved correlation. We demonstrate that global descriptors, such as mean grain size and bulk texture, are insufficient to capture growth selectivity. Instead, we find that (i) surface and GB-energy anisotropies govern thermally driven grain growth, (ii) at room temperature, applied stresses promote coarsening through grain-size-dependent yielding, and (iii) at a mild temperature, stress further enhances GB mobility by lowering the kinetic barrier for migration.

2. Methods

NC Ni thin films with a thickness of 100 nm were deposited using three different methods: (i) electron-beam evaporation (Denton Explorer) at a pressure of $\sim 10^{-6}$ Torr and deposition rate of 1.5 Å/s, (ii) DC magnetron sputtering (Kurt J Lesker PVD 200) at a rate of 2 Å/s at room temperature, and (iii) DC magnetron sputtering at a rate of 2 Å/s at 100 °C substrate temperature. The resulting film thicknesses were measured using a Dektak 150 Profilometer. Films were deposited onto patterned Si wafers defined by electron beam lithography using the photoresist SU-8 1813. Following development, metal deposition was performed, and a standard liftoff procedure was conducted by immersing the sample in acetone under sonication for 30 s, producing dog-bone-shaped specimens, followed by XeF_2 dry etch to make freestanding films. More details on the fabrication process can be found in our previous studies [25–27], including the final release procedures. For clarity, the e-beam–evaporated film is here designated Type A, while the magnetron-sputtered films with room temperature and 100 °C substrate temperatures are designated Type B and C, respectively. To create a sample with a bimodal grain-size distribution, one Type A sample was also annealed in vacuum (10^{-3} Pa) at 180 °C for 30 min.

Experiments were conducted using a 300 kV FEI Tecnai F30 TEM operated in bright-field mode; 4D-STEM measurements were performed in scanning transmission electron microscopy (STEM) mode with a convergence angle of 0.7 mrad. In situ thermal annealing experiments were carried out using DENSsolutions Wildfire P.U.H.ST.1 Heating v2 chips. For these tests, the specimen temperature was ramped to 700 °C; although the microstructure is already stable by ~300 °C, a higher annealing temperature was used to ensure that a fully stabilized state was reached before characterization. In situ straining experiments were carried out using a micro-electromechanical-system (MEMS) device [11,12,26–30]. TEM bright field imaging was carried out using a OneView CMOS camera, while 4D-STEM data were collected using a Gatan Metro 300 pixelated detector. The step size for 4D-STEM scans was selected as one-tenth of the observed $\bar{d}$ to ensure sufficient resolution in orientation mapping. To obtain statistically robust datasets for mechanical loading, multiple 4D-STEM scans were acquired per sample until at least 10,000 grains that had undergone coarsening were captured in a single experiment on the same specimen.

Mechanical loading was applied by straining the film to 4% strain (ε), after which the actuator motion was stopped to maintain a constant displacement and allow stress relaxation under tension. Due to machine compliance, the nominal strain in the film continued to increase even under constant actuator displacement. Thus, the actual loading path represented an intermediate condition between pure stress relaxation and pure creep under constant stress. This loading mode caused continued microstructural evolution, leading to a final strain exceeding 4%. Representative stress–strain curves for this loading procedure at room temperature are shown in Supplementary Fig. S1. Once the microstructure stabilized (after ~40 min), 4D-STEM data were collected. We decompose the total strain, ε, into elastic strain (ε_e) and plastic strain (ε_p), defined as $\varepsilon_e \approx \sigma/E$ and $\varepsilon_p = \varepsilon - \varepsilon_e$.

A subset of the MEMS devices with a specimen pad heater (relying on Joule heating of beams adjacent to the specimen pad) were used to perform mechanical loading at ~100 °C (see Supplementary Fig. S2). The experiments were conducted by first applying voltage to the MEMS heating pads to reach the target temperature, followed by tensile loading of the specimen (as done in the experiments at room temperature). The specimen temperature was approximated by assuming that the MEMS temperature scales with applied power (a reasonable assumption for Joule heating) and knowing the temperature-dependent microstructural response of the Ni specimen with the Wildfire heating chips. Specifically, the nc Ni film exhibited clear thermal instability when the temperature reached ~180 °C (using the wildfire heating chips). Similarly, grain growth was observed for an input voltage across the specimen pad of the MEMS device exceeding 4.3 V, indicating that this power level corresponds to a specimen temperature of ~180 °C. Similarly, under comparable vacuum conditions, Au exhibits thermal instability at ~150 °C during ex situ furnace annealing, and the same instability is triggered on the MEMS heater at applied voltages exceeding 3.6 V. Together with the Ni calibration point (~180 °C at 4.3 V), this yields an estimated specimen temperature of ~100–110 °C at 3.0 V, well below the thermal instability threshold for Ni. For simplicity, this condition is reported as ~100 °C (0.22 T_m), while noting that the absolute temperature remains approximate.

The 4D-STEM datasets were indexed using a template-matching algorithm implemented in Gatan DigitalMicrograph™ [31]. Prior to indexing, samples were processed using neighbor pattern averaging and re-indexing (NPAR) [32,33]. Orientation maps were visualized and analyzed using OIM Analysis™ (EDAX). Non-indexed points as well as regions with fewer than three contiguous pixels sharing the same orientation were excluded to ensure that only reliably indexed grains were included in the dataset.

3. Results

3.1. Initial microstructure

The as-deposited nc Ni thin films exhibit distinct initial

microstructures depending on the deposition method. Bright-field TEM images (Fig. 1a–c) confirm that all three as-deposited films are nc, with most grain sizes below 20 nm. The texture strength is quantified in multiples of random distribution (MRD) [34]. An MRD value of 1 indicates a completely random orientation, while values greater than 1 reflect preferred crystallographic alignment. Inverse pole figure (IPF) maps and data constructed from the 4D-STEM data indicate that these deposition routes yield different weak out-of-plane textures: ⟨110⟩ for Type A, mixed ⟨112⟩/⟨111⟩ for Type B, and ⟨100⟩ for Type C, with maximum texture intensities of approximately 2.7, 2.8, and 2.9 MRD, respectively (Fig. 1d–i). The in-plane orientations are essentially random, exhibiting maxima of 1.8 MRD. The elevated deposition temperature used for Type C produced a slightly broader grain size variation; therefore, additional scans were performed to ensure accurate quantification of its initial microstructure (Supplementary Fig. S3). Grain size distributions (Fig. 1j) show log-normal distributions for all films with an average grain size ($\bar{d}$) of ~10 nm. Most of the recorded nanobeam diffraction patterns were single-grain and indexed with high confidence, confirming that the grains are primarily columnar and extend through the film thickness.

Because tracking the statistical evolution of individual grains is challenging, the four dominant low-index out-of-plane orientation

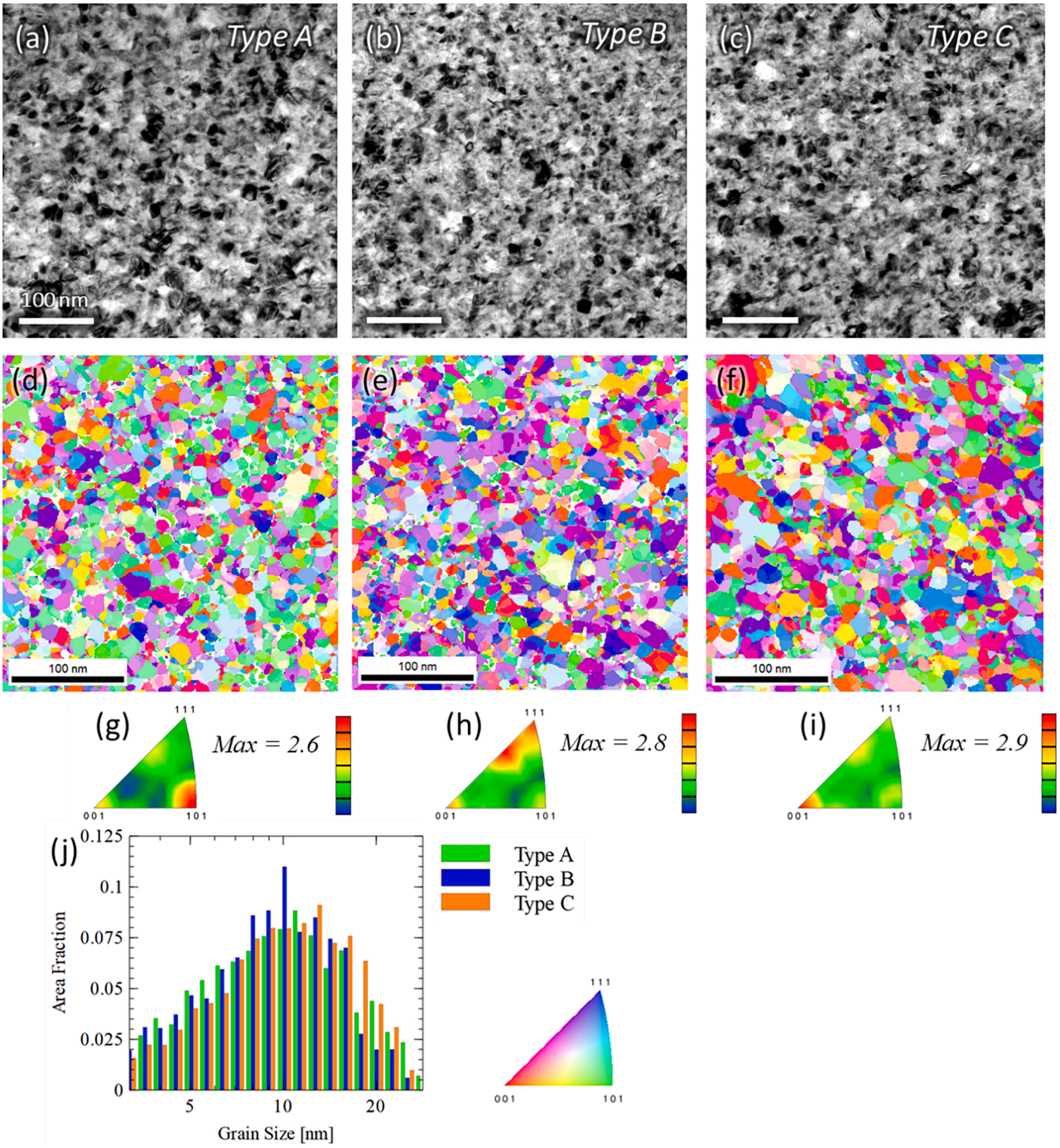

Fig. 1. (a–c) Bright-field TEM images (100 nm scale bar) of the as-deposited (a) Type A, (b) Type B, and (c) Type C, respectively. Representative (d) Type A, (e) Type B, and (f) Type C out-of-plane orientation maps derived from 4D-STEM data of characteristic regions. (g–i) Texture intensities shown in IPF triangles. (j) Area-weighted grain-size histograms for the three films centered near 10 nm.

families, ⟨111⟩, ⟨100⟩, ⟨110⟩, and ⟨112⟩, were used to statistically capture trends linking the initial grain structure with the stress/temperature-induced microstructure evolution. Although the overall grain-size distributions of the three films appear similar (Fig. 1j), the orientation-sensitive statistics reveal clear and systematic differences among the individual texture components (Table 1). In Table 1, grains were grouped within an angular tolerance of 10° from each fiber axis. The corresponding mean grain size ($\bar{d}$) and the MRD were computed for each family. Note that this grouping reflects only the statistical distribution of orientations and does not imply any intrinsic orientation-dependent properties of the material. As shown later, this classification simply provides a framework for quantitatively comparing how texture influences subsequent grain-growth behavior. According to Table 1, the Type A film exhibits similar $\bar{d}$ values across all texture components. In Type B, the ⟨111⟩ and ⟨100⟩ components are relatively large, whereas the ⟨110⟩ component is smaller. Type C exhibits a pronounced ⟨100⟩ component, with $\bar{d}$ approximately 25% larger than the other orientation families.

3.2. Microstructure evolution due to thermal annealing

Over the 30-min anneal at 700 °C, all three films developed pronounced fiber textures (an example of annealing-induced grain growth is shown in the in situ sequence in Supplementary Video S1). The post-annealing IPF maps are presented in Fig. 2a1–c1, with the corresponding texture intensity shown in Fig. 2a2–c2. The Type A film evolves into a mixed fiber texture dominated by ⟨111⟩ and ⟨100⟩ out-of-plane orientations, with a maximum intensity of ~2.5 MRD. Type B and Type C films evolve into stronger fiber textures composed almost entirely of ⟨111⟩ and ⟨100⟩ oriented grains. The grain-size distributions of the annealed films (Fig. 2d) show broadening from sub-100 nm to ~800 nm.

Table 2 summarizes the orientation-specific $\bar{d}$ and MRD values for the annealed films. The results consistently indicate that the dominant ⟨111⟩ and ⟨100⟩ components observed in the IPF maps correspond to the largest $\bar{d}$ values in their respective films.

3.3. Microstructure evolution due to mechanical loading at room temperature

3.3.1. Statistical analysis of stress-induced grain growth at room temperature

Mechanical loading was performed on all three texture variants (an example of stress-assisted grain growth is shown in the in situ sequence in Supplementary Video S2). To ensure statistical significance, 7–11 orientation maps were acquired for each specimen to capture a total population of at least 20,000 grains per film. A Type A specimen was loaded elastically to a high stress of ~1 GPa, corresponding to ε_e ~0.5% (the yield stress is ~1.4 GPa) and held for ~30 min, matching the hold duration used in other experiments. No detectable grain growth was observed under this condition, and plastic strain accumulation was negligible, confirming elastic loading. This result indicates that elastic straining alone is insufficient to activate coarsening. Instead, the grain growth observed is associated plastic deformation. The corresponding elastic and total strain values for all mechanically loaded conditions (room temperature and 100 °C, Types A–C) are summarized in Supplementary Table S3.

After straining, the orientation maps (Fig. 3a1–c1; full datasets in Supplementary Figs. S4–S6) and the corresponding IPF triangles (Fig. 3a2-c2) reveal distinct dominant orientations among the three films. Type A exhibits a weak ⟨110⟩ preference with a maximum intensity of ~2.8 MRD. Type B shows a pronounced ⟨111⟩ component reaching ~3.9 MRD, and Type C displays a dominant ⟨100⟩ orientation with a maximum of ~3.3 MRD. As shown in Fig. 3d, Type A exhibits the narrowest grain size distribution, with most grains in the 10–20 nm range, but also a rapidly decaying coarse tail extending beyond 100 nm, indicating a minor population of abnormally large grains (ALGs). Type B shows a higher $\bar{d}$, with the majority of grains ranging from 15 to 35 nm and a small population of ALGs. Type C has slightly broader distribution than Type A, with grain sizes concentrated between 15 and 25 nm. However, no ALGs larger than 100 nm were observed in Type C, as shown in the inset of Fig. 3d. Note that a direct comparison of the grain growth process among the three films is not possible, as the stress and strain relaxation required to reach a stable post-loading microstructure differ between specimens.

The orientation-resolved grain-size statistics in Table 3 are broadly consistent with the texture features described above. It should be noted that the presence of ALGs strongly affects the standard deviation. For example, in Type A, the $\bar{d}$ values are comparable across orientations except for ⟨100⟩, since the higher value and large standard deviation arise from a single rare ALG (see Supplementary Fig. S4). Type B exhibits markedly coarser ⟨111⟩ grains, consistent with its dominant ⟨111⟩ fiber and broader grain-size distribution. Type C, characterized by a strong ⟨100⟩ texture, likewise exhibits the largest average grain size in the ⟨100⟩-oriented population among the measured orientations. The coexistence of a retained fine-grain and a coarse-grain tail after mechanical loading is likely influenced by local texture and GB neighborhoods.

3.3.2. Interrupted analysis

To capture the evolution of individual grains under loading, ~300 nm × 300 nm regions in Type A and B films were tracked using interrupted 4D-STEM orientation mapping. This approach eliminates specimen-to-specimen variability and enables the same grains to be tracked through successive load–hold cycles. A type A specimen was loaded to ~1.6 GPa. During the hold period, the applied stress relaxed while the strain increased to ~12% ($\varepsilon_e \approx 0.5\%$ and $\varepsilon_p \approx 11.5\%$) due to the system compliance. The orientation maps at $\varepsilon = 12\%$ reveal a clear increase in grain size, accompanied by multiple instances of grain rotation (examples highlighted in Fig. 4a–b). The rotation angle was quantified as the symmetry-reduced disorientation between the orientations of manually matched grains in consecutive scans; the >20° threshold was chosen to identify rotations well above indexing/matching uncertainty. Among 50 grains that could be confidently matched across scans, 22 grains (44%) exhibited rotations exceeding 20°. These rotations complicate direct grain-to-grain correlation between microstructures at different states. As shown in Fig. 4e, the $\bar{d}$ increased from 9.4 ± 4.6 nm in the undeformed state to 13.9 ± 9.0 nm after loading. Despite this coarsening, the overall out-of-plane texture remained essentially unchanged. The maximum MRD in the IPF triangle is nearly identical before and after straining (Fig. 4c-d), and the area fractions of the dominant out-of-plane orientations (Fig. 4f) exhibit only minor changes. The smaller $\bar{d}$ measured in these tracked regions compared to the statistical dataset reflects the absence of ALGs within the selected local fields of view.

Fig. 5 presents interrupted 4D-STEM orientation mapping of a Type B film, tracking a ~300 nm × 300 nm region before and after loading. Three maps were acquired at sequential hold stages (Fig. 5a-c): (i) the undeformed state ($\varepsilon = 0\%$), (ii) after loading to $\varepsilon \approx 4\%$ and holding for ~30 min, during which the applied stress relaxed and the strain increased to $\varepsilon \approx 8\%$, and (iii) after a second load–hold cycle, where the strain was reloaded to $\varepsilon \approx 12\%$ and subsequently relaxed to $\varepsilon \approx 16\%$.

Table 1
Orientation-resolved average grain size in the as-deposited Ni films ($\bar{d}$ ± SD, nm) with their respective MRD values.

Orientation	Type A	Type B	Type C
⟨110⟩	9.4 ± 4.7 (2.7)	8.4 ± 5.4 (1.1)	10.0 ± 5.9 (1.0)
⟨111⟩	9.8 ± 6.1 (1.0)	11.0 ± 5.2 (2.6)	10.1 ± 4.7 (1.1)
⟨112⟩	8.6 ± 4.0 (1.5)	9.9 ± 5.4 (2.8)	10.3 ± 5.6 (1.4)
⟨100⟩	9.6 ± 5.2 (1.8)	10.2 ± 6.0 (1.8)	13.7 ± 8.7 (3.1)
Total	9.7 ± 4.6	10.1 ± 5.5	11.4 ± 4.6

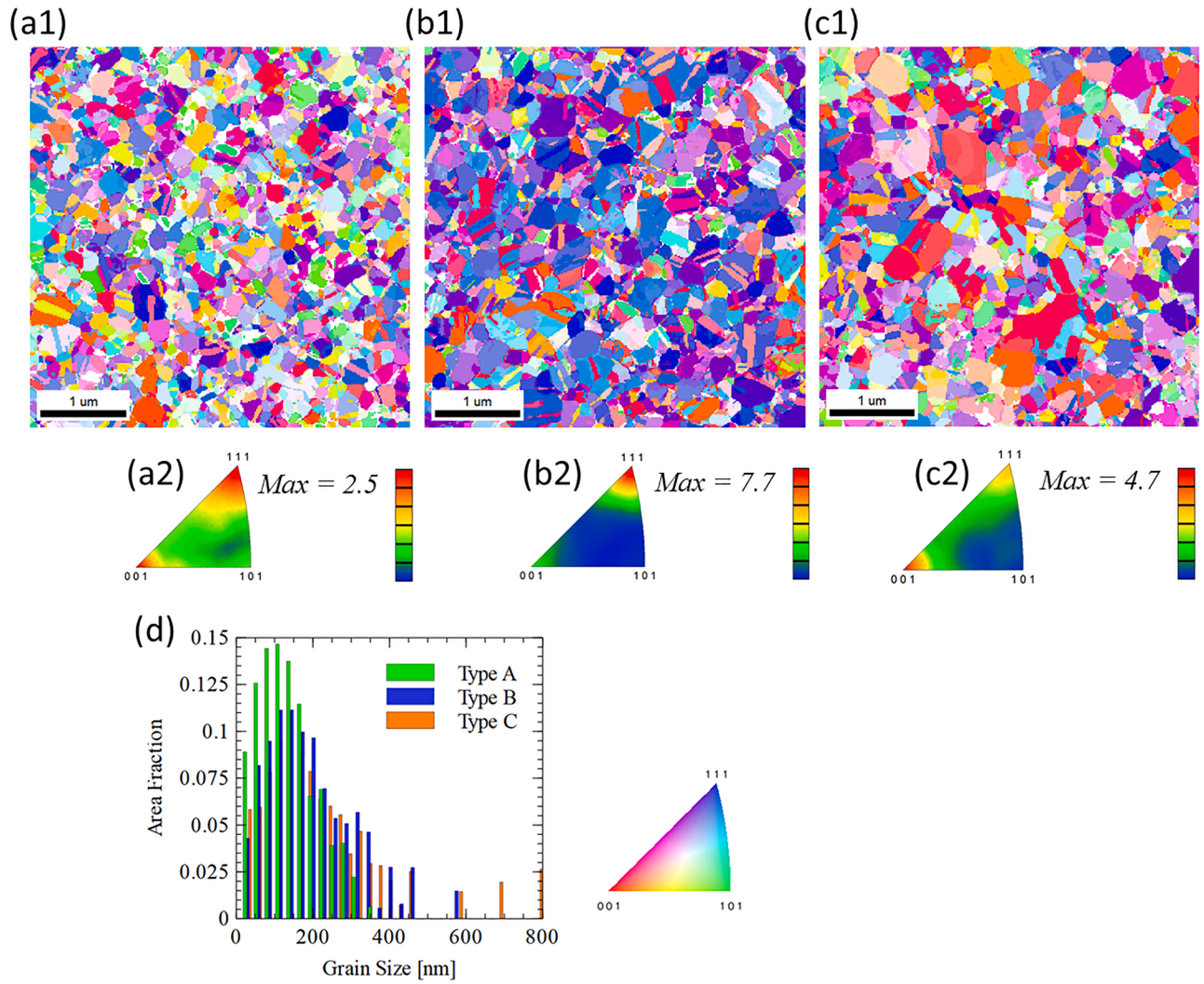

Fig. 2. Microstructure analysis of the thin films after annealing at 700 °C for 30 min: (a1–c1) Out-of-plane orientation maps obtained by 4D-STEM for (a1) Type A, (b1) Type B and (c1) Type C, respectively. (a2-c2) IPF triangles corresponding to the orientation maps directly above them with maximum MRD labeled. (d) Grain size distributions for all three materials after annealing.

Table 2
Orientation-resolved average grain size in the annealed Ni films ($\bar{d} \pm$ SD, nm) with their respective MRD values after annealing.

Orientation	Type A	Type B	Type C
⟨110⟩	139.5 ± 74.2 (0.7)	122.7 ± 61.3 (0.7)	135.5 ± 71.2 (0.7)
⟨111⟩	170.3 ± 80.7 (2.5)	250.0 ± 128.2 (7.6)	212.8 ± 108.6 (2.3)
⟨112⟩	128.9 ± 64.0 (1.3)	147.2 ± 82.2 (1.8)	172.6 ± 89.3 (1.4)
⟨100⟩	181.7 ± 98.8 (2.4)	194.9 ± 106.4 (2.4)	377.4 ± 258.4 (4.7)
Total	145.8 ± 75.4	198.7 ± 118.1	225.6 ± 70.9

Accounting for the small recoverable elastic strain at the holds, these states correspond to plastic strains of $\varepsilon_p \approx 7.6\%$ (Fig. 5b) and $\varepsilon_p \approx 15.7\%$ (Fig. 5c). The final strained microstructure (Fig. 5c) shows a slightly evolved texture compared to the initial state (Fig. 5a).

Analysis of the dominant orientations (Fig. 5d) reveals that while the MRD value of ⟨111⟩ and ⟨100⟩ components increase steadily (1.8→2.9→3.3 and 1.6→1.6→1.8, respectively), the ⟨112⟩ remains nearly constant (1.8), and the ⟨110⟩ fraction decreases from 1.2→0.8→0.5. The $\bar{d}$ increased monotonically from 10.0 ± 4.7 nm to 13.8 ± 7.2 nm, and ultimately to 18.2 ± 10.1 nm, with the corresponding distributions shown in Fig. 5e.

Fig. 5f quantifies preferential size selection under mechanical loading (up to $\varepsilon \approx 8\%$) by manually tracking and registering ~300 grains between interrupted scans (170 growing and 130 shrinking/disappearing). Each tracked grain was classified by its net area change (ΔA) between scans as "grow" (ΔA > 0) or "shrink" (ΔA < 0). Because grains smaller than ~5 nm could not be consistently identified between maps, the cumulative area-fraction distributions in Fig. 5f are constructed from the tracked population, which is predominantly composed of grains ≥ 5 nm. To avoid biasing the baseline size distribution by only considering grains that change, the "initial" distribution overlaid in Fig. 5f is obtained directly from the full initial orientation map (all grains), whereas the grow/shrink curves are normalized by the total number of tracked grains in each subset. Importantly, grains that experience significant growth at later stages were already distinguishable in the initial microstructure (Fig. 5f): the largest ~10% of grains account for ~40 % of the total area that later becomes part of the mechanically induced grown-grain population. Conversely, grains that shrink are systematically smaller (Fig. 5f) and display a strong ⟨110⟩ orientation bias, with intensities peaking at ~6.3 MRD (Fig. 5h).

The orientation maps also show frequent grain rotations, with representative examples marked by black arrows in Fig. 5a–b. Rotations are most pronounced between stages (i)→(ii): ~30% (91 grains) rotate by >20°, and the average angle of rotation is 6.2°. Between stages (ii)→(iii), rotation is substantially reduced; among 50 grains that could be

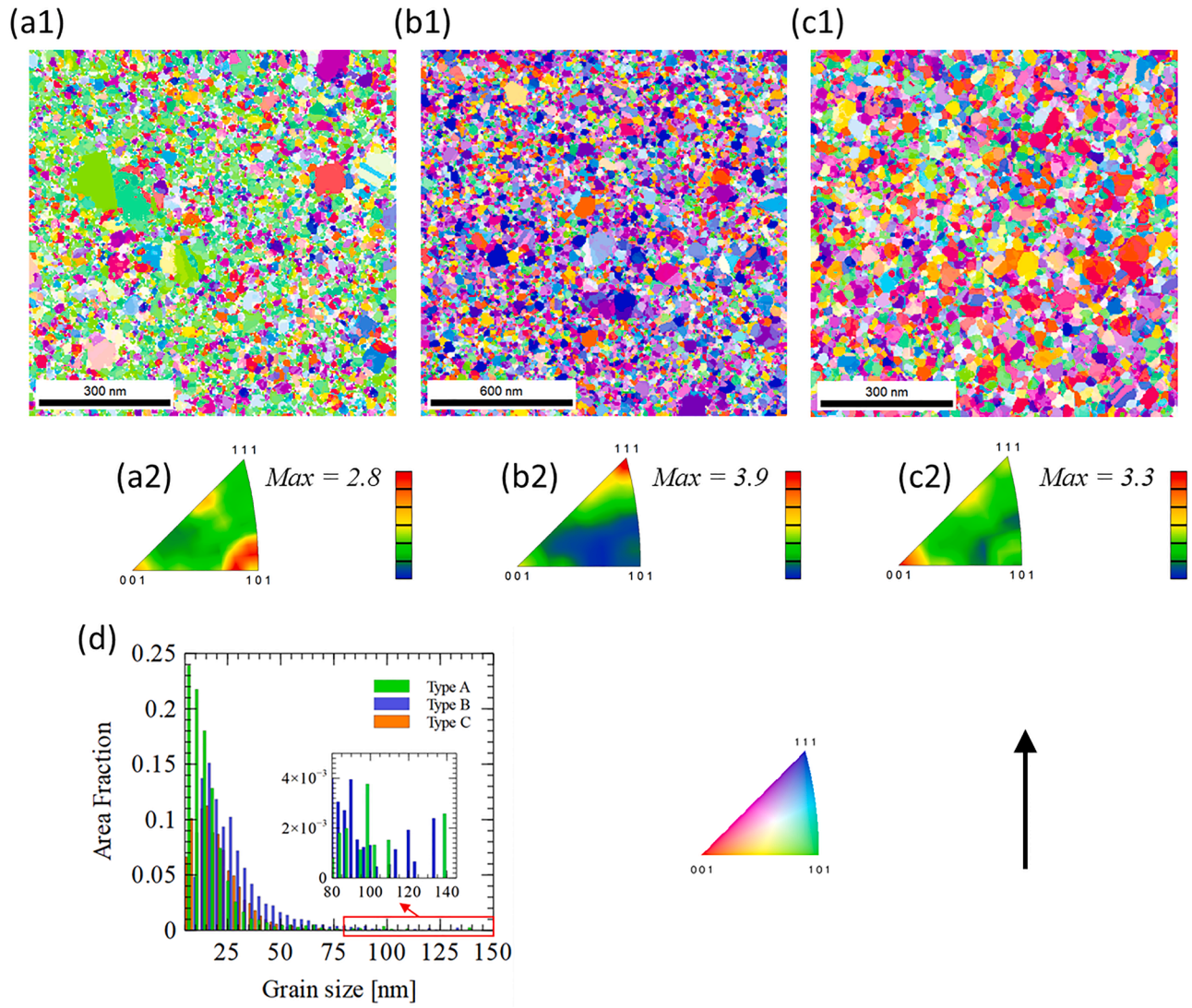

Fig. 3. Representative 4D-STEM IPF-Z orientation maps of the films after loading at room temperature: (a1) Type A, (b1) Type B, (c1) Type C. (a2-c2) IPF triangles of statistical datasets compiled from all scans for each film type (scan × ~10 for each): (a2-c2) after loading, (d) area-weighted grain-size distributions for Types A–C (inset: magnified view of the red-boxed tail, 80–150 nm, highlighting abnormally large grains).

Table 3
Orientation-resolved average grain size in the 100 nm Ni films ($\bar{d} \pm$ SD, nm) with their respective MRD from mechanical loading at room temperature.

Orientation	Type A	Type B	Type C
⟨110⟩	15.0 ± 13.5 (2.8)	19.8 ± 11.9 (0.5)	16.2 ± 8.7 (0.9)
⟨111⟩	15.7 ± 12.1 (1.0)	33.5 ± 23.7 (4.1)	18.1 ± 8.9 (1.0)
⟨112⟩	15.2 ± 11.4 (1.5)	25 ± 14.6 (2.4)	18.1 ± 10.3 (1.4)
⟨100⟩	20.6 ± 25.6 (1.8)	28.7 ± 21.0 (2.4)	24.2 ± 14.4 (3.4)
Total	17.2 ± 15.3	27.7 ± 17.5	20.1 ± 11.6

confidently matched, none rotate by >20°, and the average rotation angle is ~1.5°. These large apparent rotations (>20°) in both experiments (Figs. 4 and 5) are generally observed in grains that also undergo pronounced growth or shrinkage (i.e., typically the initially larger or smaller grains). This indicates that the measured rotations primarily reflect GB-mediated microstructural evolution, rather than simple rigid-body lattice rotation of an otherwise unchanged grain, consistent with prior reports of coupled GB motion and grain rotation in nc microstructures [35].

In a complementary experiment on a bimodal microstructure produced by annealing, boundary motion under mechanical loading was confined to the pre-existing ALGs, while the surrounding nc matrix remained essentially immobile (Supplementary Fig. S7 and Supplementary Video S3). Interrupted analysis was not performed on Type C films, as their grain growth was too small to track on a grain-by-grain basis and the pronounced spatial heterogeneity in the initial texture would render localized measurements unrepresentative.

3.4. Microstructure evolution due to mechanical loading at 100 °C

The statistical comparison experiments for all three films were further repeated at 100 °C, again comparing the initial microstructures to the ones obtained after straining to ε = 4% and holding. Prior to loading, the as-deposited microstructures were confirmed to remain unchanged upon heating. That is, no grain growth occurs at 100 °C in the absence of an applied load. Following the same procedure as in the room-temperature experiments, approximately ten orientation maps of comparable field of view were analyzed for each film (step size ~$\bar{d}$/10). Representative orientation maps after the load–hold are shown in Fig. 6a1–c1 (full datasets in Supplementary Figs. S8–S10). From the corresponding IPF triangles (Fig. 6a2-c2), Type A exhibits dominant peaks near ⟨112⟩ and ⟨100⟩ with a maximum intensity of ~2.5 MRD in the overall film. Type B shows a strong ⟨111⟩ component reaching ~4.3

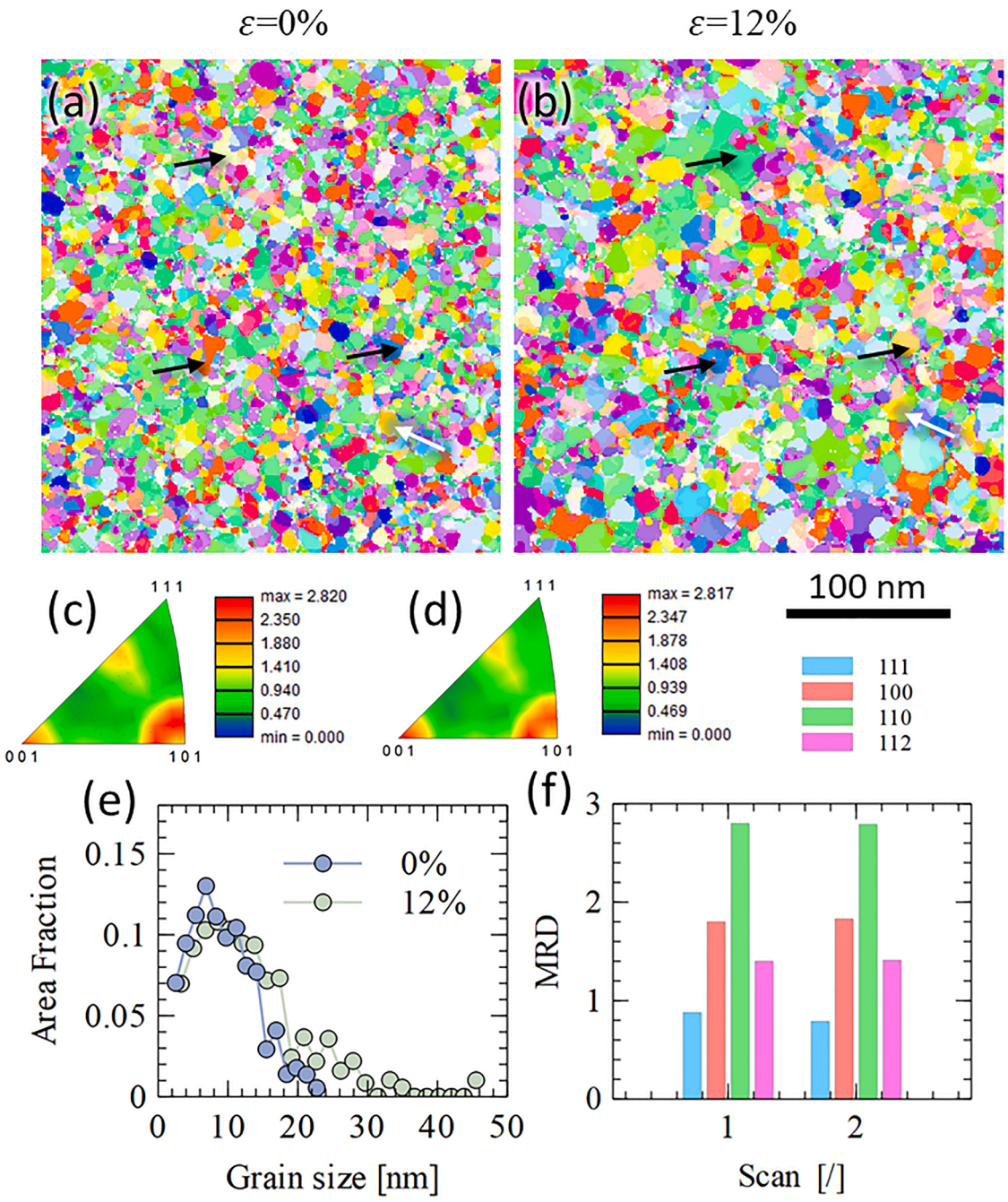

Fig. 4. Interrupted 4D-STEM analysis of a Type A film. (a) Orientation map in the undeformed state. (b) Orientation map of the same area after mechanical loading for 30 min. The white arrow indicates a reference point in the two scans. (c,d) Corresponding IPF triangles, expressed in MRD, are shown below each corresponding orientation map. (e) Grain-size distributions before and after straining, showing an increase in average grain size from 9.4 nm to 13.9 nm. (f) MRD intensities of the four dominant out-of-plane orientations for each scan.

MRD; and Type C displays a pronounced ⟨100⟩ fiber with a maximum of ~3.6 MRD. Grain-size histograms (Fig. 6d) quantify the extent of grain growth. The distributions of Types A and B shift toward larger grain sizes compared to Type C, with a more pronounced 80–150 nm shoulder and ALGs extending up to ~280 nm. The normalized grain-size distributions are provided in Supplementary Fig. S11.

The orientation-resolved grain-size statistics in Table 4 are consistent with the corresponding IPF triangles (Fig. 6a2-c2): Type B and Type C exhibit the highest intensities of ⟨111⟩ and ⟨100⟩ grains, respectively. In contrast, Type A also shows unusually large ⟨111⟩ grains with relatively low size dispersion. Such selective coarsening indicates a growth mode that could be different from other orientations, in which this orientation is preferentially selected, so these grains grow much larger at the expense of the surrounding matrix.

4. Discussion

The primary objective of this study is to compare thermally and mechanically induced microstructural evolution in Ni thin films as a function of their initial texture, in order to identify and decouple the dominant driving forces governing grain growth. We first distinguish the growth trends arising from the distinct thermal and mechanical loading histories, and then analyze the underlying driving forces inferred from these contrasting behaviors.

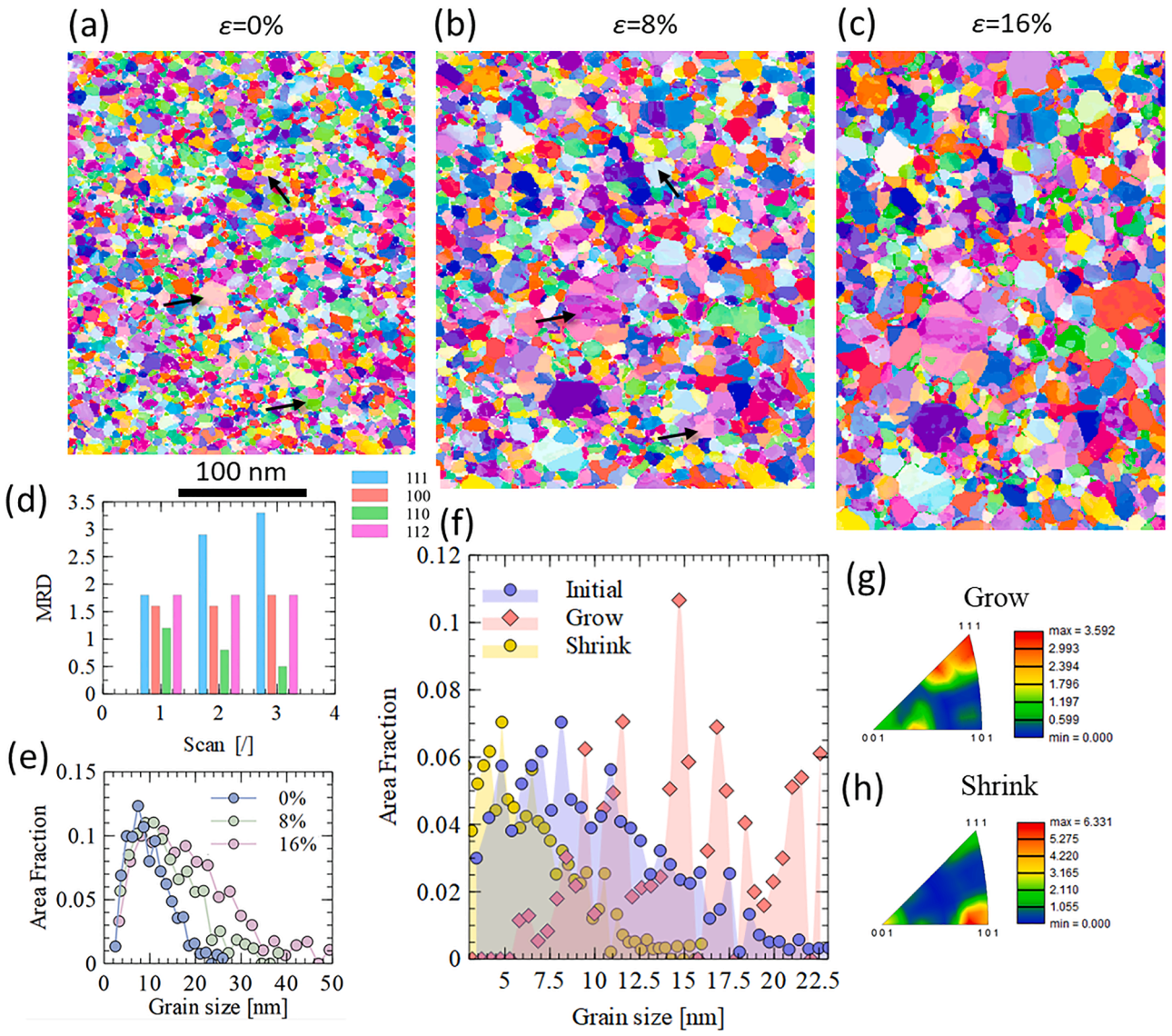

Fig. 5. Interrupted 4D-STEM analysis of grain growth in a Type B film subjected to mechanical loading. Orientation maps (a-c) correspond to three stages: undeformed ($\varepsilon = 0\%$), after load and 30 min hold that reaches $\varepsilon \approx 8\%$, and after a second load–hold reaching $\varepsilon \approx 16\%$. Some occurrences of grain rotation are marked by black arrows in (a-b). (d) MRD evolution for different out-of-plane orientation families for the three scans. (e) Grain size distributions for the three different strain levels. (f) Cumulative area fraction plotted versus grain size for the undeformed microstructure: "initial" includes all grains at $\varepsilon = 0\%$; "grow" and "shrink" refer to grains identified as growing or shrinking upon mechanical loading (b). (g-h) IPF pole density maps for the grains that (g) grow and (h) shrink.

Grain-growth behavior is evaluated by tracking the evolution of texture components in each film type for two key reasons. First, because these specimens are thin-film geometries with a large free-surface area, grains with out-of-plane orientations that possess lower surface energies (e.g., ⟨111⟩ and ⟨100⟩ in fcc crystals) reduce the total system energy. Second, different texture families exhibit statistically distinct initial grain-size distributions. Grouping grains by their texture components thus provides a convenient and meaningful way to compare growth behavior among grain populations with different starting sizes. Although out-of-plane texture itself may not directly dictate stress-induced grain growth, it serves as a useful surrogate parameter that links initial grain-size statistics to the experimentally observed growth trends.

4.1. Texture evolution

4.1.1. Thermally-induced texture evolution

Upon thermal annealing, all three films exhibit pronounced strengthening of their ⟨111⟩ and ⟨100⟩ fiber textures along with extensive annealing-induced twinning, consistent with the tendency to minimize surface and grain-boundary energies [36,37]. Among the low-index planes in Ni, the ⟨111⟩ surface has the lowest energy (~1.95 J m^{-2}), followed by the ⟨100⟩ surface (~2.25 J m^{-2}), with ⟨110⟩ being substantially higher [38]. Consequently, grains with ⟨111⟩ out-of-plane orientations grow most favorably, and ⟨100⟩-oriented grains are also promoted relative to higher-energy orientations. After annealing, Type A exhibits a slightly broader ⟨111⟩ spread than Types B and C, whereas Type C contains a larger fraction of ⟨100⟩ grains. These differences likely arise from their distinct initial textures and boundary configurations, which interact and coevolve during grain growth [37].

4.1.2. Stress-induced texture evolution at room temperature

Stress-induced grain growth (for applied stress above the yield stress) produces texture evolution that is highly dependent on the initial texture state. As illustrated in Fig. 7, the out-of-plane IPF triangles for the films after mechanical loading are shown first for all grains in each type of

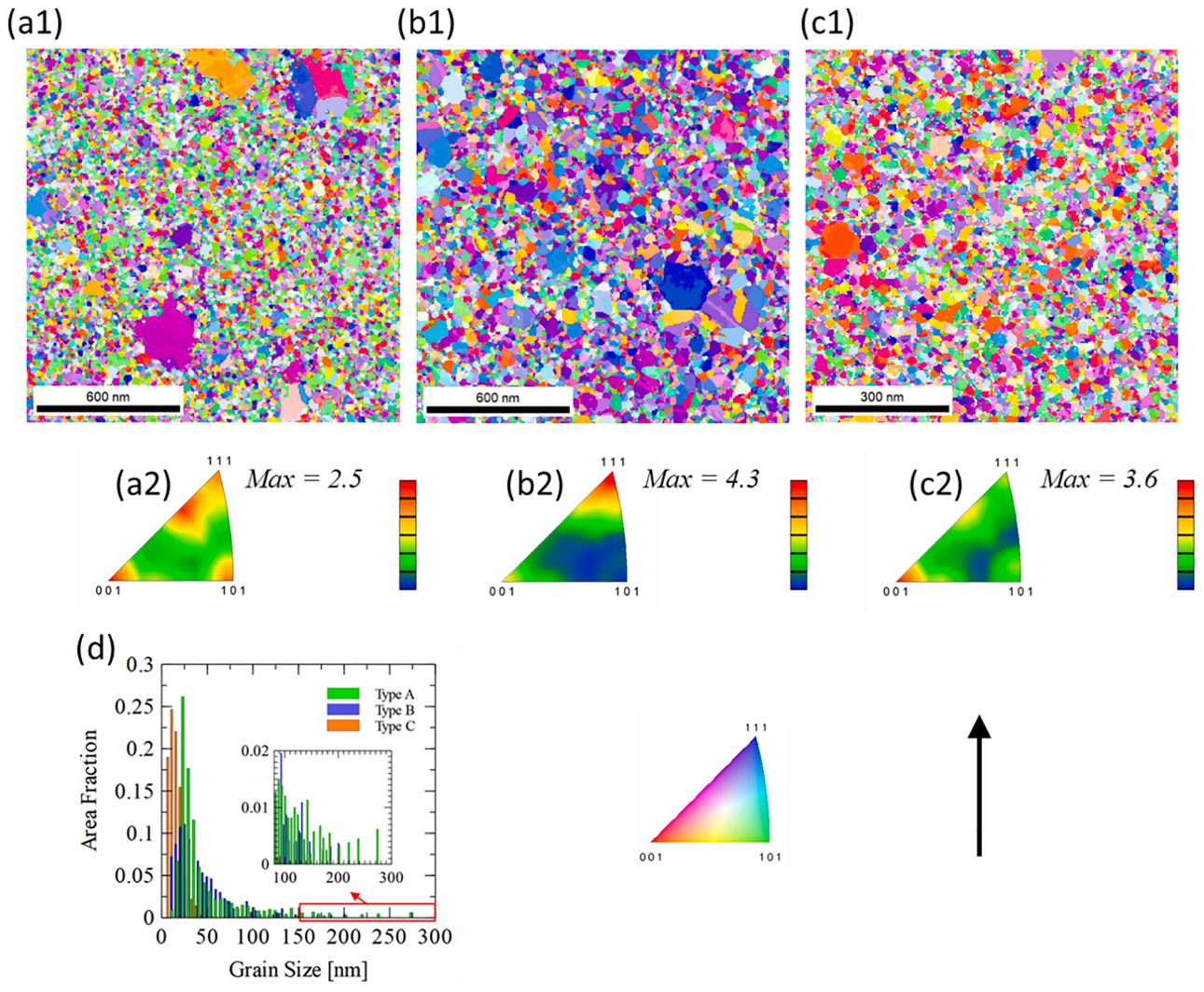

Fig. 6. Representative 4D-STEM IPF-Z orientation maps of the films after mechanical loading at 100 °C: (a1) Type A, (b1) Type B, (c1) Type C. (a2-c2) Statistical datasets compiled from all scans for each film type (scan × ~10 for each): (a2-c2) IPF triangles after mechanical loading, (d) area-weighted grain-size distributions for Types A–C (inset: magnified view of the red-boxed tail, 80–300 nm, highlighting abnormally large grains).

Table 4
Orientation-resolved average grain size in the Ni films ($\bar{d}$ ± SD, nm) with their respective MRD values from mechanical loading at 100 °C.

Orientation	Type A	Type B	Type C
⟨110⟩	25.8 ± 20.0 (1.7)	19.8 ± 11.9 (0.5)	13.3 ± 6.4 (1.0)
⟨111⟩	57.4 ± 6.3 (1.5)	33.5 ± 23.7 (4.7)	14.7 ± 6.7 (1.2)
⟨112⟩	27.7 ± 25.9 (2.5)	54.1 ± 14.6 (2.3)	14.8 ± 7.4 (1.7)
⟨100⟩	36.8 ± 44.4 (2.4)	37.8 ± 28.2 (2.4)	19.9 ± 13.1 (3.6)
Total	33.2 ± 36.6	50.5 ± 31.7	16.0 ± 8.5

film (type A-C in Fig. 7a1–c1, respectively) and then for only the coarsened subset (Fig. 7a2-c2). Coarsened grains are defined as those whose final sizes ($\bar{d}$) exceed approximately twice their as-deposited mean size. The cutoff sizes were 20 nm for Types A and B and 23 nm for Type C (see Supplementary Table S1 for quantitative fractions and $\bar{d}$).

Type A, which exhibited an initially uniform grain-size distribution across its texture components, shows minimal texture evolution. Its weak ⟨110⟩ fiber remains essentially unchanged, with a maximum intensity of 2.8 MRD in both the overall film and the coarsened subset (Fig. 7a1 and a2). In Type B, where ⟨111⟩-oriented grains were initially larger on average than the other texture families, stress-assisted growth becomes orientation sensitive. The weak ⟨112⟩ component in the as-deposited state (~2.9 MRD) transforms into a dominant ⟨111⟩ fiber after loading, reaching 3.9 MRD in the overall film and 4.3 MRD in the coarsened subset (Fig. 7b1 and b2). Type C also shows strong orientation-dependent coarsening. Because its ⟨100⟩-oriented grains were initially larger than other orientations, mechanical loading amplifies the preexisting ⟨100⟩ fiber, increasing from 3.3 MRD in the full film to 5.4 MRD in the coarsened population (Fig. 7c1 and c2). Collectively, these trends indicate that stress-assisted grain growth leaves the texture of Type A nearly unchanged, whereas Types B and C undergo pronounced sharpening along ⟨111⟩ in Type B and ⟨100⟩ in Type C.

4.1.3. *Combined effect of stress and temperature on texture evolution*

When mechanical loading was applied at a moderate temperature of ~100 °C (insufficient to trigger grain growth in the absence of applied load), the orientation selectivity became even more pronounced; see Fig. 8 and Supplementary Table S2. In Type A, a previously absent ⟨111⟩ component begins to appear, while the ⟨112⟩ and ⟨100⟩ components decrease in relative intensity. The overall film exhibits a maxima of ~2.5 MRD for both ⟨112⟩ and ⟨100⟩, while the coarsened subset sharpens to ~2.8 MRD (Fig. 8a1 and a2). The transition from "no ⟨111⟩ selection" at room temperature to "emergent ⟨111⟩ selection" at 100 °C indicates that

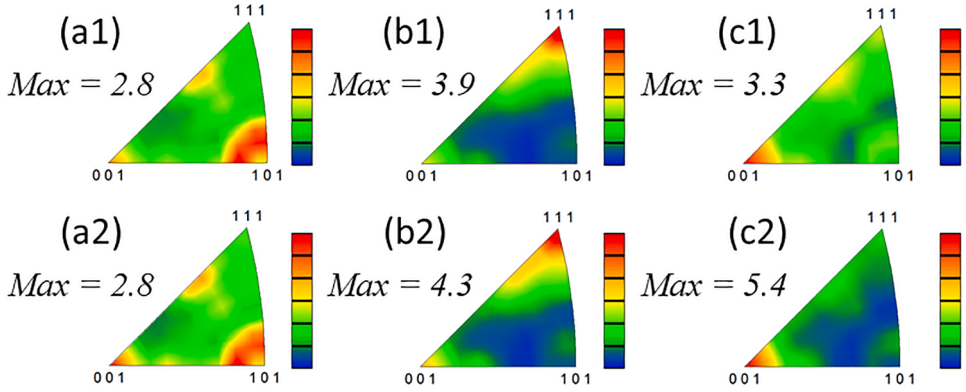

Fig. 7. Post deformation IPF triangles constructed from the 4D-STEM data. (a1–c1) Overall film texture for Types A–C, respectively. (a1-c1) correspond to those shown in Fig. 3(a2-c2). (a2-c2) Texture of grains that grew during mechanical loading for Types A–C, respectively. Color denotes MRD values; the reported numerical values indicate the maximum MRD value.

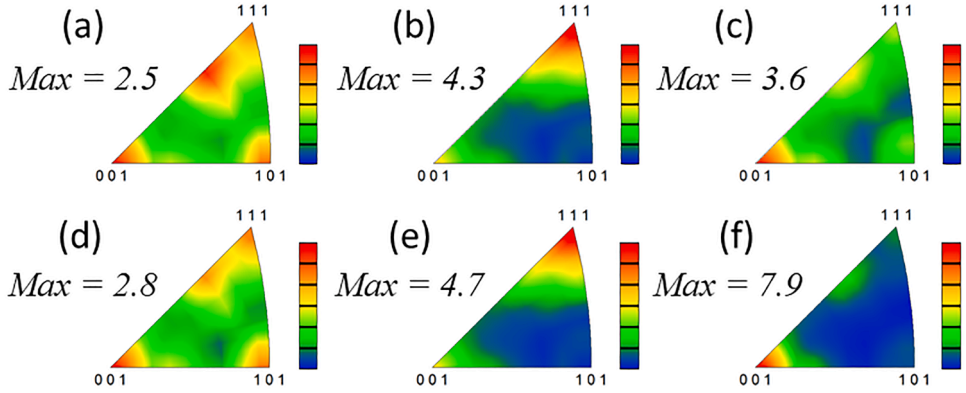

Fig. 8. Texture summary after mechanical loading at 100 °C shown by out-of-plane IPF triangles. (a1–c1) Overall-film texture for Types A–C. (a1-c1) correspond to those shown in Fig. 6(a2–c2). (a2–c2) Texture of grains that grew during mechanical loading for Types A–C. Color denotes MRD values; the reported numerical values indicate the maximum MRD value.

the moderate temperature biases the energetics and activates a new ⟨111⟩ orientation preference in Type A. While Type B, which develops a dominant ⟨111⟩ fiber under room temperature loading (as shown in Fig. 7b1 and b2, 3.9 MRD overall, 4.3 MRD subset), undergoes further intensification at 100 °C loading, reaching ~4.3 MRD overall and ~4.7 MRD for the coarsened grains (Fig. 8b1 and b2). Thus, a moderate increase in temperature amplifies the existing ⟨111⟩ preference already established under room-temperature loading for Type B. Type C exhibits

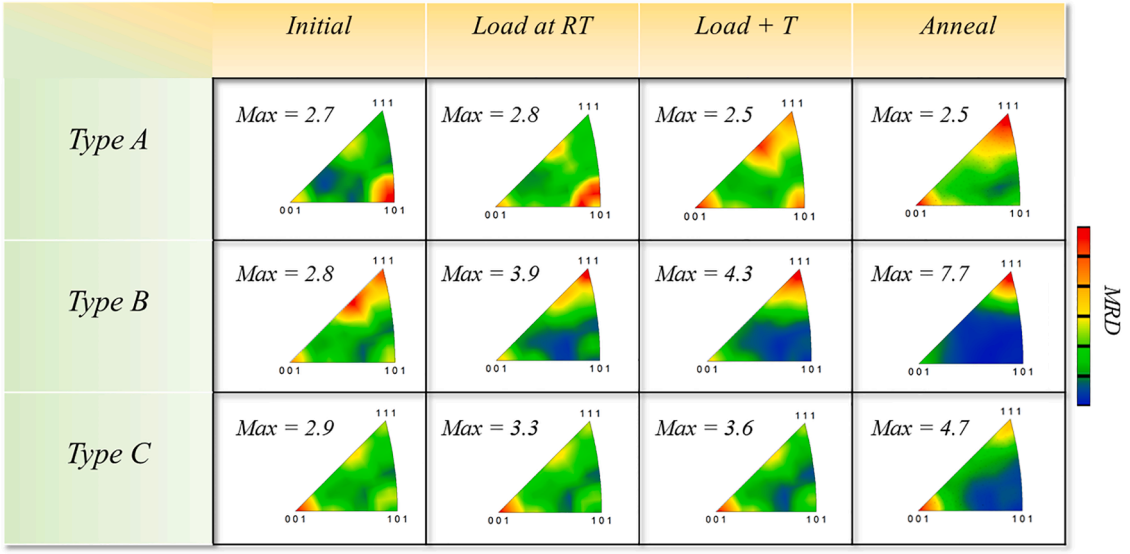

Fig. 9. IPF triangles summarizing the texture evolution from the initial state to three processing conditions: Load at RT (loading to ~4% strain followed by holding at room temperature), Load + T (loading to ~4% strain followed by holding at 100 °C), and Anneal (thermal annealing at 700 °C without applied stress).

a similar thermally enhanced trend as Type B: the ⟨100⟩ fibers in Type C, which are already strengthened during room-temperature mechanical loading (3.3 MRD overall, 5.4 MRD subset), intensifies further at 100 °C, reaching ~3.6 MRD overall and ~7.9 MRD in the coarsened subset (Fig. 8c1 and c2).

As summarized in Fig. 9, the textures that emerge under different environmental conditions follow clearly distinct evolution paths. During mechanical loading (applied stress above yield stress) at room temperature, Type A retains its initial weak textures with minimal change, whereas Types B and C reorient toward their size-favored components (⟨111⟩ and ⟨100⟩, respectively). Under thermal annealing, all films evolve toward strong ⟨111⟩/⟨100⟩ textures. Mechanical loading at 100 °C yields an intermediate response, producing partial sharpening of these same preferred orientations. This mixed character is most evident in Type A, where annealing-favored orientations are superimposed with those promoted by room-temperature loading. In contrast, Types B and C show strong overlap between mechanically and thermally favored texture components, such that the primary differences manifest mainly in the magnitude of the MRD intensities rather than in the identity of the preferred orientations. The summary of the corresponding pole figures for these conditions are also provided in Supplementary Fig. S12. For clarity, each IPF triangle is independently scaled, and the corresponding maximum MRD value is indicated next to each map.

4.1.4. GB evolution

In addition to the orientation selection described above, the boundary network also evolves during grain growth. Because the Ni films contain predominantly high-angle boundaries (disorientation >15°) of various tilt and twist character, the total boundary energy of a given microstructure cannot be directly quantified (the disorientation distribution of all the experiments are summarized in Supplementary Fig. S13). Instead, we track the evolution of the twin network by identifying Σ3 boundaries and their associated Σ9 variants before and after thermal or mechanical loading.

As shown in Fig. 10a–c, room-temperature mechanical loading leads to modest but clearly film-dependent changes in boundary character. The Σ3 length fraction decreases from 0.152 to 0.133 (–12.5%) in Type A and from 0.216 to 0.181 (–16.2%) in Type B, but increases slightly from 0.168 to 0.182 (+8.3%) in Type C. The Σ9 fraction remains small and changes only marginally. Although these differences cannot be attributed to a single mechanism, the content of special boundaries is expected to be coupled to texture evolution: shifts in orientation populations naturally modify the frequency of twin-related variants [39]. Consistent with this interpretation, mechanical loading at room temperature produces only small, film-specific adjustments (Fig. 10).

Mechanical loading at a moderate temperature produces boundary distribution changes that are clearly distinct from the room-temperature case, but not as prominent as those produced by annealing (Fig. 10). In contrast to RT mechanical loading, where the Σ3 length fraction decreases in Types A and B and changes only slightly in Type C, loading at 100 °C leads to a consistent increase in Σ3 content across all three films: from 0.152 to 0.176 (+15.8%) in Type A, from 0.216 to 0.227 (+5.1%) in Type B, and from 0.168 to 0.179 (+6.5%) in Type C (Fig. 10a–c). Annealing produces a much stronger increase in Σ3, from 0.152 to 0.290 (+90.8%) in Type A, from 0.216 to 0.386 (+78.7%) in Type B, and from 0.168 to 0.280 (+66.7%) in Type C, while the Σ9 length fraction also increases consistently across all three film types. This progression in boundary statistics (RT loading < load+T < annealing) is consistent with the texture evolution summarized in Fig. 9, where loading at a moderately elevated temperature promotes partial development of annealing-associated texture components (primarily ⟨111⟩/⟨100⟩), whereas annealing produces the strongest sharpening of these preferred orientations.

4.1.5. Summary of microstructure evolution trends

Overall, our observations reveal two distinct trends of microstructure-evolution: (i) a grain-size-associated growth bias, in which grains initially larger than the film average tend to grow preferentially, and (ii) a texture-selection trend, in which ⟨111⟩/⟨100⟩ components become increasingly prominent. The former dominates during room temperature deformation, where grains initially larger than the film average tend to grow at the expense of smaller ones. This behavior is reflected in the texture evolution. The texture components associated with relatively large initial grains (e.g., ⟨100⟩ grains in Type C) strengthen after mechanical deformation, whereas those associated with relatively small grains (e.g., ⟨110⟩ grains in Type B) weaken. This concept is illustrated schematically in Fig. 11. In Case 1 (Fig. 11a-c), when all orientation families begin with comparable grain size distributions, coarsening is uniform, and the out-of-plane texture is essentially "locked" from the initial state. The Type A films demonstrate this behavior. In Case 2 (Fig. 11d-f), different texture components have different average grain sizes. Under applied load, the larger-grain families grow and ultimately increase their area fraction/dominate, while the smaller-grain families shrink. This process shifts the overall texture toward those initially larger populations (Type B/C behavior).

The second trend, the preferential growth of low surface energy grains, becomes dominant once the temperature is elevated. Under mechanical loading at 100 °C, grain growth is already governed primarily by this thermally driven mechanism, which operates even more strongly during pure thermal annealing at higher temperatures (e.g., 700 °C). Consequently, the samples develop a texture intermediate between the stress-selected state at room temperature and the annealed state (Fig. 9), and the Σ3 twin-boundary fraction also increases monotonically (Fig. 10), mirroring its evolution under pure annealing.

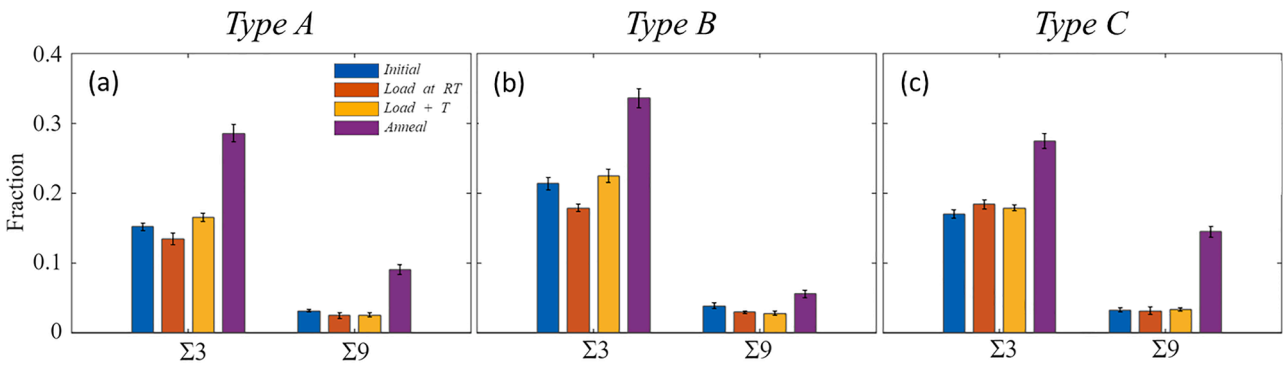

Fig. 10. Special-boundary statistics for Types A–C. (a–c) Length fractions of Σ3 and Σ9 boundaries in the as-deposited state and after room-temperature mechanical loading, mechanical loading at 100 °C, and thermal annealing.

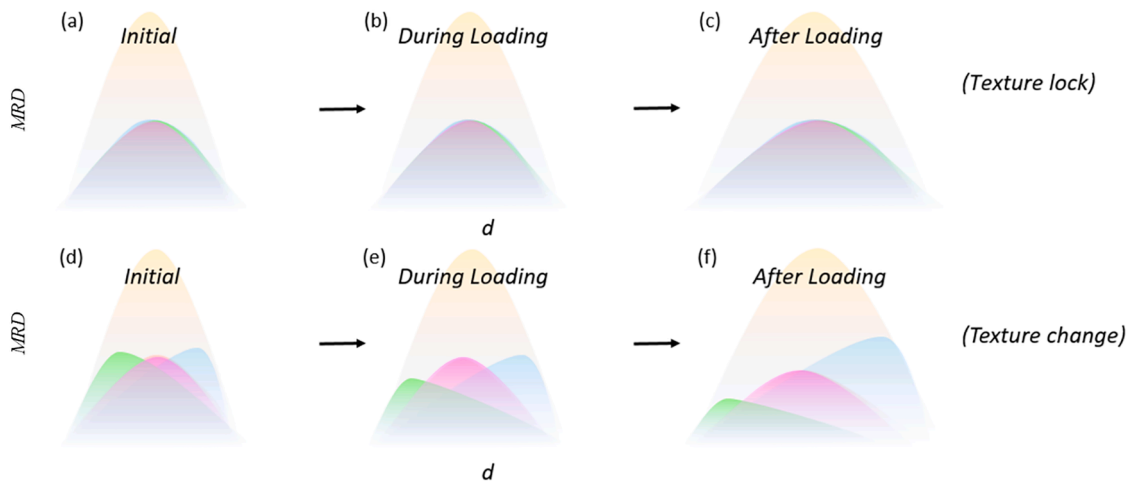

Fig. 11. Orientation-resolved schematic illustrating two types of stress-induced grain-growth behavior. (a–c) All orientation families start with comparable log-normal grain-size distributions, as shown in (a), plotted with the intensity (MRD), where MRD denotes the density (multiples of random) of the given family. Grain growth shifts the distributions to larger sizes while preserving their relative weights, so the texture is retained (b,c). (d–f) Evolution of orientation-biased coarsening: grains with initially different orientation-dependent size distributions (d) develop growth responses (e, f) that change the texture. The yellow area denotes the overall grain-size distribution, while the colored curves represent orientation-resolved subsets.

4.2. Effects of stress and temperature on grain growth

4.2.1. General considerations

From a global energy perspective, grain growth can be understood as a process of reducing the total free energy of the system. In polycrystalline Ni thin films, this reduction occurs due to different dominant driving forces. First, the system can reduce GB energy through conventional capillarity-driven coarsening, i.e., by reducing total GB area and, when GB energies are anisotropic, by preferentially replacing higher-energy boundaries with lower-energy boundaries [40–43]. Second, in thin-film geometries, surface-energy anisotropy can bias orientation-selective grain growth: grains with lower-energy surface normal (e.g., fcc ⟨111⟩ and ⟨100⟩, with representative surface energies of 1.94 and 2.21 J m^{-2}, respectively [38]) can grow preferentially, thereby reducing the total surface-energy contribution without changing the film geometry [44–46]. Third, under external loading, mechanical effects become important [47,48]. Because the experiments conducted in this study are displacement-controlled, the elastic energy stored in the film scales as $W \approx \frac{1}{2}E\varepsilon^2$. Thus, at a fixed applied strain, the system can reduce W by increasing the fraction of elastically compliant grains aligned with the loading direction [3,48,49], or through plastic dissipation, where stress-assisted growth of yielding grains consumes stored mechanical energy.

Importantly, however, the reduction of total system energy does not necessarily imply that grains with lower elastic strain energy density must grow at the expense of those with higher elastic strain energy density. As shown in prior simulations [49], elastically softer grains may grow even when they exhibit higher stored elastic strain energy density under displacement-controlled loading. This apparent paradox arises because the driving force for boundary migration is not determined solely by local elastic energy density, but by the change in total system energy, including both elastic strain energy and stress work associated with boundary motion.

From a local energy perspective, GB migration is governed by configurational forces acting on the boundary. The classical capillarity effect, proportional to boundary curvature and energy, drives boundary motion that reduces total GB energy. Under applied stress, shear-coupled GB migration provides a stress-assisted kinetic pathway, allowing boundary motion to proceed with coupled shear deformation. At the same time, elastic anisotropy creates orientation-dependent differences in stored elastic energy, which can bias boundary motion toward replacing elastically stiffer grains with more compliant ones [48]. Once plasticity begins, grain size introduces a further effect through grain-size-dependent yielding, enabling local plastic accommodation that can further promote boundary motion. Together, these global and local perspectives provide a unified energetic framework that explains our experimental observations of grain-size-driven growth, surface-energy-induced texture sharpening, stress-assisted coarsening, and the evolution of special boundary networks in Ni thin films.

Regarding the effects of temperature and stress, grain growth at high temperatures is usually governed by the reduction of total surface and GB energy through curvature-driven GB migration. In this process, boundary motion reduces interfacial area and tends to favor the development/expansion of low-γ_s surface facets, while low-γ_{GB} boundaries (e.g., twin boundaries) are preferentially retained within the evolving network (and may increase in relative fraction as higher-energy/more mobile boundaries are removed), where γ_s and γ_{GB} denote the free-surface energy and grain-boundary energy, respectively. When mechanical loading is applied, grain growth can be influenced by two complementary contributions, arising from elastic and plastic deformation. In the purely elastic regime, the orientation-dependent elastic response alters the configurational force acting on grain boundaries through differences in stored strain energy and in the stress-work associated with GB motion, thereby biasing boundary migration. Once the plastic regime initiates, a second mechanism arises from grain-size-dependent yielding. Owing to Hall–Petch strengthening, larger grains relax earlier through plastic slip [11]. This process drives GBM from plastically softer toward harder grains. Such differential yielding may also arise from orientation-dependent Schmid factors, as grains with higher factors require lower external stresses to activate slip. While curvature- and stored-energy define the thermodynamic driving force for GBM, the migration rate is also governed by the boundary mobility, which can be influenced by mechanical loading. Under an applied shear stress τ, the mechanical work τV^* (where $V^*$is the activation volume) lowers the activation energy, thus increasing boundary mobility. Below, we review each case of observed grain growth and the corresponding evidence reported in the literature [11,12], including modeling and *in situ* experiments that aim to disentangle these effects. Throughout the discussion, we frame our analysis around the four dominant out-of-plane fiber components—⟨111⟩, ⟨100⟩, ⟨110⟩ and ⟨112⟩—present in the three films.

4.2.2. Stress-driven grain growth at room temperature

The final microstructures after mechanical loading at room temper-

ature exhibit texture responses that depend on the initial microstructure. These results might be interpreted in terms of the possible orientation-selective driving forces governing grain growth. Schmid factors (m) were calculated from the measured crystal orientations by projecting the loading direction onto each {111}⟨110⟩ slip system. For each pixel, we computed $m = |\cos\phi\cos\lambda| = |(\hat{n}\cdot\hat{L})(\hat{s}\cdot\hat{L})|$, where $\hat{n}$ is the slip-plane normal, $\hat{s}$ is the slip direction, and $\hat{L}$ is the unit vector along the applied loading axis. The values show minimal change with deformation from their initial states: Type A 0.45 ± 0.05 → 0.45 ± 0.04, Type B 0.45 ± 0.04 → 0.45 ± 0.04, and Type C 0.45 ± 0.04 → 0.46 ± 0.04. The small shifts and strongly overlapping distributions indicate that orientation-dependent resolved shear stress does not provide a dominant bias for the observed grain growth.

Although grain growth is not observed at room temperature at stresses below the yield stress, it can occur once the applied stress is sufficiently high to activate GB motion. If the primary role of stress were merely to enhance boundary mobility, i.e., to overcome kinetic barriers to migration without altering the thermodynamic selection criteria, the resulting texture evolution would be expected to resemble that produced by thermal annealing. In that case, low-surface-energy orientations such as ⟨111⟩ and ⟨100⟩ would be favored, consistent with Fig. 2 and prior studies [50–52]. However, our experimental observations show little to no sharpening of the low-surface-energy ⟨111⟩ texture in either Type A or Type C, and the Σ3 boundary fraction does not increase appreciably. These results indicate that surface and grain-boundary energy anisotropy does not play a leading role in determining stress-driven grain growth behavior at room temperature.

Under applied tension, grains with less elastic energy are expected to outgrow their neighbors, with early experimental evidence of this effect [53] dating back to the 1950s. To identify the elastically soft orientation in a polycrystal thin film, we modeled a representative cylindrical grain of cubic symmetry embedded in a homogeneous polycrystal subjected to uniaxial tension. The diffraction elastic constants along loading direction were evaluated by combining the classical Eshelby inclusion solution with the self-consistent solution, based on the formulation derived in our previous work [54]. If elastic anisotropy were the primary selection mechanism, the largest grains would converge toward the most compliant orientations. However, the orientation-resolved modulus analysis shows no evidence that elastically compliant grains preferentially coarsen (see Supplementary Figure S14 and its description in the Supplementary Material). This concept appears more relevant under high cycle loading conditions, where a recent study of UFG Ni films under low applied loads revealed preferential coarsening of grains oriented with ⟨100⟩ along the loading direction [3].

At room temperature, coarsening is observed only after yielding and is therefore best described as plasticity-assisted, size-biased coarsening, rather than orientation-driven selection. The primary correlation observed in our experiments is the influence of grain size on coarsening behavior. As shown in Fig. 5f for the Type B film, grains that grew during mechanical loading were predominantly those in the upper tail of the initial size distribution (>60% area fraction of the coarsened grains were initially larger than 15 nm). This size bias is also evident in the GBM behavior observed in the pre-annealed bimodal grain structure (Fig. S7), where pre-grown coarse grains further expanded during subsequent loading, while the surrounding nc matrix remained unchanged. This explains why the Type A film retains its initial texture during stress-driven grain growth, whereas the textures of the Type B and C films evolve.

4.2.3. Stress-assisted grain growth at 100 °C

At 100 °C, mechanical loading produces an intermediate response between the purely size-biased behavior observed at ambient temperature and the surface or grain-boundary-energy–controlled grain growth that occurs during thermal annealing (Fig. 9). It is important to emphasize that the applied temperature was sufficiently low to prevent any spontaneous GB motion in the absence of stress. Therefore, the observed GB migration at this temperature is attributed to stress-assisted activation rather than thermal effects alone. As shown in Figs. 7–11, the emergence of large ⟨111⟩ grains and an increased fraction of low-energy boundaries at 100 °C indicates that, while stress continues to supply a modest grain-size-dependent driving component, the coarsening becomes increasingly governed by interfacial-energy minimization, favoring low-γ_s orientations and low-γ_{GB} boundaries. Mechanistically, this behavior can be rationalized by the increased boundary mobility, as the mechanical work τV^* lowers the activation energy of boundary motion [55,56]. Consequently, at 100 °C, where thermal activation alone is insufficient to solely drive grain growth, the additional mechanical work term τV^* significantly decreases the kinetic limitation and accelerates boundary motion. The relative dominance of stress-driven versus thermally-driven migration would depend on both the temperature and the magnitude of the applied stress.

4.3. Effects of deposition methods

In e-beam evaporation, atoms impinge on the substrate surface with low kinetic energy (<1 eV) and perpendicular trajectories, resulting in a limited surface mobility and a comparatively less dense microstructure [57,58]. In contrast, sputter deposition involves higher adatom energies (~10 eV), which enhances surface diffusion and leads to a slightly denser film [57,58]. Oxygen/solute segregation could modify grain-boundary energy and mobility and thereby affect the extent and kinetics of grain growth, with oxygen preferentially segregating to the boundaries [59,60]. Because the oxygen level is below the detection limit of our TEM–EDX measurements, we cannot fully exclude a contribution from solute effects. However, we do not expect solute segregation to dictate the size-based selection trends observed in this study. A definitive assessment of boundary solute content would require atom probe tomography (APT), which is beyond the scope of the present work. Such measurements would be valuable in future studies to directly evaluate how dilute solute segregation affects grain boundary migration. The various adatom kinetics contribute to the development of the various out-of-plane textures observed in Fig. 2. The higher deposition temperature used for Type C could also potentially lead to more stabilized boundary structures [59,60] that could affect the extent of grain growth. Although impurity segregation at GBs has been shown to impede grain growth during annealing by inducing boundary pinning [61], such effects are unlikely to be significant here due to the high purity nickel source (99.995%).

Grain-boundary grooving at the free surface can impose a geometric/kinetic constraint, which may limit the overall extent of coarsening [62]. However, grooving does not introduce a mechanism that would selectively bias growth toward initially larger grains; therefore, it is not expected to account for the size-based selection trends discussed here. Prior experience with comparable ~100 nm films shows that groove depths in the as-deposited films are generally shallow (~5 nm [29]), and should not have a large effect on the mechanical properties.

5. Conclusion

The effects of temperature and mechanical loading on grain growth in nc Ni films were investigated both statistically and on a grain-by-grain basis using MEMS-based in situ TEM experiments. By testing films with varying initial microstructures, we show that thermally driven and stress-dominated grain growth follow distinct pathways depending on the initial texture and environment. Specifically,

- Annealing at high temperature (700 °C) leads to conventional thermally driven grain growth through a surface and GB energy–minimization route, strengthening the ⟨111⟩ or ⟨100⟩ fiber texture and increasing Σ3 twins in all films.

- Mechanical loading at room temperature causes stress-dominated grain growth: coarsening occurs for larger grains in the initial size distribution, indicating size-dependent selection rather than orientation preference. Consequently, stress-driven texture evolution occurs only when the initial grain is orientation-biased (Types B and C), whereas films with orientation-independent grain size (Type A) maintain their original texture. This behavior is attributed to grain size dependent yielding.
- Mechanical loading at a moderate temperature (100 °C) assists thermally driven grain growth, producing mixed selection: larger grains continue to grow, while stress-enhanced GB mobility promotes the growth of low-surface-energy orientations, partially steering the texture toward that seen in annealed samples.

These results reveal the competing roles of temperature, stress and initial texture in controlling microstructural stability in NC metal thin films. They also demonstrate the growing capability of TEM as a big-data technique for statistically representative texture quantification.

CRediT authorship contribution statement

Yichen Yang: Writing – original draft, Investigation, Conceptualization. **Yazhuo Liu:** Writing – review & editing, Conceptualization. **Ting Zhu:** Writing – review & editing, Conceptualization. **Olivier Pierron:** Writing – review & editing, Conceptualization. **Josh Kacher:** Writing – review & editing, Conceptualization.

Declaration of competing interest

The authors declare that they have no known competing financial interests or personal relationships that could have appeared to influence the work reported in this paper.

Acknowledgments

The authors gratefully acknowledge support by the U.S. Department of Energy (DOE), Office of Science, Basic Energy Sciences (BES) Materials Science and Engineering (MSE) Division under Award #DE-SC0018960.

Supplementary materials

Supplementary material associated with this article can be found, in the online version, at doi:10.1016/j.actamat.2026.122305.

References

[1] B.L. Boyce, H.A. Padilla, Anomalous fatigue behavior and fatigue-induced grain growth in nanocrystalline nickel alloys, Metall. Mater. Trans. A 42 (7) (2011) 1793–1804.
[2] T.A. Furnish, D.C. Bufford, F. Ren, A. Mehta, K. Hattar, B.L. Boyce, Evidence that abnormal grain growth precedes fatigue crack initiation in nanocrystalline Ni-Fe, Scr. Mater. 143 (2018) 15–19.
[3] A. Barrios, Y. Zhang, X. Maeder, G. Castelluccio, O. Pierron, T. Zhu, Abnormal grain growth in ultrafine grained Ni under high-cycle loading, Scr. Mater. 209 (2022) 114372.
[4] J. Greiser, P. Müllner, E. Arzt, Abnormal growth of "giant" grains in silver thin films, Acta Mater. 49 (6) (2001) 1041–1050.
[5] G.D. Hibbard, J.L. McCrea, G. Palumbo, K.T. Aust, U. Erb, An initial analysis of mechanisms leading to late stage abnormal grain growth in nanocrystalline Ni, Scr. Mater. 47 (2) (2002) 83–87.
[6] S.-J.L. Kang, 9 - abnormal grain growth, in: S.-J.L. Kang (Ed.), Sintering, Butterworth-Heinemann, Oxford, 2005, pp. 117–135.
[7] P. Sonnweber-Ribic, P.A. Gruber, G. Dehm, H.P. Strunk, E. Arzt, Kinetics and driving forces of abnormal grain growth in thin Cu films, Acta Mater. 60 (5) (2012) 2397–2406.
[8] D.S. Gianola, S. Van Petegem, M. Legros, S. Brandstetter, H. Van Swygenhoven, K. J. Hemker, Stress-assisted discontinuous grain growth and its effect on the deformation behavior of nanocrystalline aluminum thin films, Acta Mater. 54 (8) (2006) 2253–2263.
[9] D.S. Gianola, D. Farkas, M. Gamarra, M.-R. He, The role of confinement on stress-driven grain boundary motion in nanocrystalline aluminum thin films, J. Appl. Phys. 112 (12) (2012) 124313.
[10] D.S. Gianola, D.H. Warner, J.F. Molinari, K.J. Hemker, Increased strain rate sensitivity due to stress-coupled grain growth in nanocrystalline Al, Scr. Mater. 55 (7) (2006) 649–652.
[11] S. Stangebye, K. Ding, Y. Yang, T. Zhu, O. Pierron, J. Kacher, Grain size effects on stress-assisted grain boundary migration in polycrystalline Au thin films under tension, Acta Mater. 297 (2025) 121330.
[12] S. Stangebye, Y. Zhang, S. Gupta, E. Hosseinian, F. Yu, C. Barr, K. Hattar, O. Pierron, T. Zhu, J. Kacher, Grain growth of nanocrystalline aluminum under tensile deformation: a combined in situ TEM and atomistic study, Materialia 16 (2021) 101068.
[13] R. Gautier, F. Mompiou, O. Renk, C. Coupeau, N. Combe, G. Seine, M. Legros, Quantifying grain boundary deformation mechanisms in small-grained metals, Nature 648 (8093) (2025) 327–332.
[14] B. Wang, M.T. Alam, M.A. Haque, Grain growth in nanocrystalline nickel films at low temperature and stress, Scr. Mater. 71 (2014) 1–4.
[15] T.A. Furnish, A. Mehta, D. Van Campen, D.C. Bufford, K. Hattar, B.L. Boyce, The onset and evolution of fatigue-induced abnormal grain growth in nanocrystalline Ni–Fe, J. Mater. Sci. 52 (1) (2017) 46–59.
[16] J. Han, D.J. Srolovitz, M. Salvalaglio, Disconnection-mediated migration of interfaces in microstructures: I. continuum model, Acta Mater. 227 (2022) 117178.
[17] J. Han, S.L. Thomas, D.J. Srolovitz, Grain-boundary kinetics: a unified approach, Prog. Mater. Sci. 98 (2018) 386–476.
[18] E.A. Ellis, M. Chmielus, M.-T. Lin, H. Joress, K. Visser, A. Woll, R.P. Vinci, W. L. Brown, S.P. Baker, Driving forces for texture transformation in thin Ag films, Acta Mater. 105 (2016) 495–504.
[19] S.L. Thomas, K. Chen, J. Han, P.K. Purohit, D.J. Srolovitz, Reconciling grain growth and shear-coupled grain boundary migration, Nat. Commun. 8 (1) (2017) 1764.
[20] J.W. Cahn, Y. Mishin, A. Suzuki, Coupling grain boundary motion to shear deformation, Acta Mater. 54 (19) (2006) 4953–4975.
[21] J.W. Cahn, Y. Mishin, A. Suzuki, Duality of dislocation content of grain boundaries, Philos. Mag. 86 (25–26) (2006) 3965–3980.
[22] M. Legros, D.S. Gianola, K.J. Hemker, In situ TEM observations of fast grain-boundary motion in stressed nanocrystalline aluminum films, Acta Mater. 56 (14) (2008) 3380–3393.
[23] M. Jin, A.M. Minor, E.A. Stach, J.W. Morris, Direct observation of deformation-induced grain growth during the nanoindentation of ultrafine-grained Al at room temperature, Acta Mater. 52 (18) (2004) 5381–5387.
[24] K.H. Blixt, H. Hallberg, Phase field crystal modeling of grain boundary migration: mobility, energy and structural variability, Acta Mater. 297 (2025) 121318.
[25] E. Hosseinian, O.N. Pierron, Correction: quantitative in situ TEM tensile fatigue testing on nanocrystalline metallic ultrathin films, Nanoscale 7 (26) (2015) 11468–11470.
[26] S. Stangebye, X. Liu, L. Daza Llanos, Y. Yang, T. Zhu, J. Kacher, O. Pierron, Comparison of electrical sensing and image analysis for in situ transmission electron microscopy nanomechanical testing of thin films, Thin Solid Films 787 (2023) 140125.
[27] S. Stangebye, Y. Zhang, S. Gupta, T. Zhu, O. Pierron, J. Kacher, Understanding and quantifying electron beam effects during in situ TEM nanomechanical tensile testing on metal thin films, Acta Mater. 222 (2022) 117441.
[28] L. Daza-Llanos, S. Stangebye, E.J. Lang, K. Hattar, O. Pierron, J. Kacher, Influence of irradiation damage on stress-assisted grain growth in ultrafine grained Au thin films using in situ transmission electron microscopy mechanical testing, Mater. Sci. Eng. 947 (2025) 149256.
[29] S. Gupta, S. Stangebye, K. Jungjohann, B. Boyce, T. Zhu, J. Kacher, O. Pierron, In situ TEM measurement of activation volume in ultrafine grained gold, Nanoscale 12 (2020).
[30] S. Stangebye, K. Ding, Y. Zhang, E. Lang, K. Hattar, T. Zhu, J. Kacher, O. Pierron, Direct observation of grain-boundary-migration-assisted radiation damage healing in ultrafine grained gold under mechanical stress, Nano Lett. 23 (8) (2023) 3282–3290.
[31] R. Brunelli, Matching variable patterns, template matching techniques in computer vision 2009, pp. 113-124.
[32] S.I. Wright, M.M. Nowell, S.P. Lindeman, P.P. Camus, M. De Graef, M.A. Jackson, Introduction and comparison of new EBSD post-processing methodologies, Ultramicroscopy 159 (2015) 81–94.
[33] D.J. Rowenhorst, P.G. Callahan, Y. Yang, J. Nakamura, W. Lenthe, J. Kacher, Non-local denoising for 4D STEM orientation mapping, Microsc. Microanal. 31 (Supplement_1) (2025).
[34] H.J. Bunge, 3 - orientation distributions, in: H.J. Bunge (Ed.), Texture Analysis in Materials Science, Butterworth-Heinemann, 1982, pp. 42–46.
[35] Y. Tian, X. Gong, M. Xu, C. Qiu, Y. Han, Y. Bi, L.V. Estrada, E. Boltynjuk, H. Hahn, J. Han, D.J. Srolovitz, X. Pan, Grain rotation mechanisms in nanocrystalline materials: multiscale observations in Pt thin films, Science 386 (6717) (2024) 49–54.
[36] U. Klement, M. Da Silva, W. Skrotzki, On the orientations of abnormally grown grains in nanocrystalline Ni and Ni–Fe, J. Microsc. 230 (3) (2008) 455–463.
[37] J. Kacher, K. Hattar, I.M. Robertson, Initial texture effects on the thermal stability and grain growth behavior of nanocrystalline Ni thin films, Mater. Sci. Eng. 675 (2016) 110–119.
[38] W.-B. Zhang, C. Chen, S.-Y. Zhang, Equilibrium crystal shape of Ni from first principles, J. Phys. Chem. C 117 (41) (2013) 21274–21280.

[39] D.B. Bober, A. Khalajhedayati, M. Kumar, T.J. Rupert, Grain boundary character distributions in nanocrystalline metals produced by different processing routes, Metall. Mater. Trans. A 47 (3) (2016) 1389–1403.
[40] G.S. Rohrer, I. Chesser, A.R. Krause, S.K. Naghibzadeh, Z. Xu, K. Dayal, E.A. Holm, Grain boundary migration in polycrystals, Annu. Rev. Mater. Res. 53 (2023) 347–369.
[41] J.D. Niño, O.K. Johnson, Influence of grain boundary energy anisotropy on the evolution of grain boundary network structure during 3D anisotropic grain growth, Comput. Mater. Sci. 217 (2023) 111879.
[42] G.S. Rohrer, Grain boundary energy anisotropy: a review, J. Mater. Sci. 46 (18) (2011) 5881–5895.
[43] Z. Xu, C.M. Hefferan, S.F. Li, J. Lind, R.M. Suter, F. Abdeljawad, G.S. Rohrer, Energy dissipation by grain boundary replacement during grain growth, Scr. Mater. 230 (2023) 115405.
[44] C.V. Thompson, Grain growth in thin films, Annu. Rev. Mater. Res. 20 (1990) 245–268.
[45] C.V. Thompson, Structure evolution during processing of polycrystalline films, Annu. Rev. Mater. Res. 30 (2000) 159–190.
[46] C.C. Wong, H.I. Smith, C.V. Thompson, Surface-energy-driven secondary grain growth in thin Au films, Appl. Phys. Lett. 48 (5) (1986) 335–337.
[47] C.V. Thompson, R. Carel, Stress and grain growth in thin films, J. Mech. Phys. Solids 44 (5) (1996) 657–673.
[48] M. Tonks, P. Millett, Phase field simulations of elastic deformation-driven grain growth in 2D copper polycrystals, Mater. Sci. Eng. 528 (12) (2011) 4086–4091.
[49] M. Tonks, P. Millett, W. Cai, D. Wolf, Analysis of the elastic strain energy driving force for grain boundary migration using phase field simulation, Scr. Mater. 63 (11) (2010) 1049–1052.
[50] J.L. Walter, Control of texture in magnetic material by surface energy, J. Appl. Phys. 36 (3) (1965) 1213–1220.
[51] F. Ma, J.-M. Zhang, K.-W. Xu, Surface-energy-driven abnormal grain growth in Cu and Ag films, Appl. Surf. Sci. 242 (1) (2005) 55–61.
[52] V. Weihnacht, W. Brückner, Abnormal grain growth in {111} textured Cu thin films, Thin Solid Films 418 (2) (2002) 136–144.
[53] P.A. Beck, P.R. Sperry, Strain induced grain boundary migration in high purity aluminum, J. Appl. Phys. 21 (2) (1950) 150–152.
[54] Y. Zhang, W. Chen, D.L. McDowell, Y.M. Wang, T. Zhu, Lattice strains and diffraction elastic constants of cubic polycrystals, J. Mech. Phys. Solids 138 (2020) 103899.
[55] N.F. Mott, Slip at grain boundaries and grain growth in metals, Proc. Phys. Soc. 60 (4) (1948) 391–394.
[56] T. Zhu, J. Li, S. Yip, Atomistic reaction pathway sampling: the nudged elastic band method and nanomechanics applications, Nano Cell Mech. (2013) 311–338.
[57] E. Lugscheider, C. Barimani, C. Wolff, S. Guerreiro, G. Doepper, Comparison of the structure of PVD-thin films deposited with different deposition energies, Surf. Coat. Technol. 86-87 (1996) 177–183.
[58] N. Mahne, M. Čekada, M. Panjan, Energy distribution of sputtered atoms explored by SRIM simulations, Coatings 13 (2023) 1448.
[59] J. Hu, Y.N. Shi, X. Sauvage, G. Sha, K. Lu, Grain boundary stability governs hardening and softening in extremely fine nanograined metals, Science 355 (6331) (2017) 1292–1296.
[60] A. Hasnaoui, H. Van Swygenhoven, P.M. Derlet, On non-equilibrium grain boundaries and their effect on thermal and mechanical behaviour: a molecular dynamics computer simulation, Acta Mater. 50 (15) (2002) 3927–3939.
[61] Y.M. Wang, S. Cheng, Q.M. Wei, E. Ma, T.G. Nieh, A. Hamza, Effects of annealing and impurities on tensile properties of electrodeposited nanocrystalline Ni, Scr. Mater. 51 (11) (2004) 1023–1028.
[62] H.J. Frost, C.V. Thompson, D.T. Walton, Simulation of thin film grain structures—I. Grain growth stagnation, Acta Metall. Mater. 38 (8) (1990) 1455–1462.